


Large eddy simulation of soot formation and oxidation for different ambient temperatures and oxygen levels

Journal Article**Author(s):**

Zhang, Min; Ong, Jiun Cai; Pang, Kar Mun; Bai, Xue-Song; [Walther, Jens Honoré](#) 

Publication date:

2022-01-15

Permanent link:

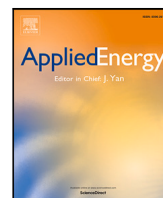
<https://doi.org/10.3929/ethz-b-000517279>

Rights / license:

[Creative Commons Attribution 4.0 International](#)

Originally published in:

Applied Energy 306(B), <https://doi.org/10.1016/j.apenergy.2021.118094>



Large eddy simulation of soot formation and oxidation for different ambient temperatures and oxygen levels[☆]

Min Zhang^a, Jiun Cai Ong^a, Kar Mun Pang^b, Xue-Song Bai^c, Jens H. Walther^{a,d,*}

^a Department of Mechanical Engineering, Technical University of Denmark, 2800 Kgs. Lyngby, Denmark

^b MAN Energy Solutions, Tegholmegade 41, 2450 Copenhagen, Denmark

^c Division of Fluid Mechanics, Lund University, P.O. Box 118, S221 00 Lund, Sweden

^d Computational Science and Engineering Laboratory, ETH Zürich, CH-8092, Zürich, Switzerland

ARTICLE INFO

Keywords:

Spray A
Soot formation
Soot oxidation
Ambient temperature
Oxygen levels

ABSTRACT

This paper presents the numerical study of soot formation and oxidation processes across different ambient temperatures (900 K, 1000 K, and 1100 K) and oxygen levels (15% and 21% O₂) using large eddy simulation coupled with a two-equation soot model. The predicted ignition delay time, lift-off length and soot distribution show good agreements with the corresponding experimental data. A stronger oxidation of the precursor (C₂H₂) in the 21% O₂ cases results in a lower C₂H₂ formed, as compared to the 15% O₂ cases. The increasing ambient temperature leads to the fuel-richer region (roughly equivalence ratio > 1.6) becoming more favorable for C₂H₂ formation and, consequently, soot formation. This is more apparent in the 15% O₂ cases due to a weaker oxidation of C₂H₂ via O and OH radicals. As a result, the difference in the soot mass between the 15% and 21% O₂ cases becomes larger as the ambient temperature increases. The effects of ambient temperature and O₂ level on soot sub-processes are investigated. In addition to the flame temperature, OH mass and soot surface area are the dominant parameters in the oxidation processes via OH and O₂ at varying O₂ levels, respectively.

1. Introduction

Diesel engines have been widely used in the transportation sectors due to their high thermal efficiency and fuel economy. However, soot emissions from diesel engines remain as a main concern since it brings negative impacts to our health and the environment. Different strategies have been developed to reduce soot emissions, such as low temperature combustion [1–3]. Numerous works have been carried out to better understand the soot formation and oxidation processes when these strategies are employed [4–9].

Experimental studies were carried out to gain a better insight into the in-cylinder soot formation processes [4,5]. Shen et al. [10] investigated the soot particles in a heavy duty diesel engine at high exhaust gas recirculation (EGR) levels. They found that an increasing EGR level leads to a higher soot mass formation. An investigation of soot oxidation at varying EGR levels in diesel engines was carried out by Gallo et al. [6], in which they found that hydroxyl radicals (OH) are the dominant oxidizer. Meanwhile, notable efforts were devoted to the study of soot formation during the diesel spray combustion process in a constant volume chamber with controllable temperature and pressure,

which are used to mimic diesel engine-like conditions [11,12]. In recent years, Spray A from the Engine Combustion Network (ECN) has gained the most attention, in which *n*-dodecane (C₁₂H₂₆) fuel is injected into a constant volume chamber through an injector nozzle with diameter of 90 μm. Skeen et al. [7] utilized the extinction-based imaging to study the soot process over a range of diesel engine-like operating conditions: 900 K to 1200 K under 15% and 21% oxygen (O₂) levels. The study demonstrated that the difference in the soot mass between these two O₂ levels becomes larger as the ambient temperature increases. However, the reason behind this increasing difference in the soot mass was not presented. Cenker et al. [8] investigated the effect of varying ambient temperatures (900 K and 1000 K) and O₂ levels (13% to 21%) on soot formation and oxidation in Spray A using laser-induced incandescence imaging. Only the change of the global soot mass trend with respect to varying ambient temperatures and O₂ levels was presented. Their findings showed a monotonic increase in the soot mass when the ambient temperature increases, but a non-monotonic increase of the soot mass as the ambient O₂ level increases. However, the effects of the ambient temperatures and O₂ levels on soot

[☆] The short version of the paper was presented at ICAE2020, Dec 1–10, 2020. This paper is a substantial extension of the short version of the conference paper.

* Corresponding author at: Department of Mechanical Engineering, Technical University of Denmark, 2800 Kgs. Lyngby, Denmark.
E-mail address: walther@mavt.ethz.ch (J.H. Walther).

sub-processes, such as inception, surface growth, and oxidation, are not fully examined. This is likely due to the limitation in the measuring technologies to obtain additional information, e.g., the distribution of soot-relevant species and the contribution of each soot sub-process.

In terms of numerical studies, computational fluid dynamics (CFD) coupled with chemical kinetic and soot models, once validated, can provide additional information that cannot be obtained in the experiment. The effects of different ambient O₂ levels (13%, 15%, and 21%) on soot formation at an ambient temperature of 900 K were investigated by Pei et al. [13]. They suggested that the strategies aiming for soot reducing need to be adjusted according to different O₂ levels. Mukut et al. [14] used a semi-empirical two-equation soot model and a detailed method of moments (MOM) soot model to study the effects of O₂ levels on soot formation. It was found that the peak soot volume fraction (SVF) increases with increasing O₂ levels. For the study of soot at different ambient temperatures, the trend where the soot mass increases with increasing ambient temperature is captured in many studies [15–17]. Gong et al. [17] investigated the soot formation at two different ambient temperatures (900 K and 1000 K) using large eddy simulation (LES). They pointed out that the difference in the soot formation under different ambient temperatures is mainly due to the difference in the local composition of mixtures.

It should be noted that the aforementioned works were solely focused on either the effects of ambient temperatures or the effect of ambient O₂ levels on soot formation. For the study of soot formation across different ambient temperatures and O₂ levels, Pandurangi et al. [18] investigated the soot onset process using Lagrangian particle tracking method under different ambient temperatures (850 K, 900 K and 1000 K), and O₂ levels (13%, 15%, and 21%). Wang et al. [19] developed a reduced *n*-dodecane-PAH (polycyclic aromatic hydrocarbons) mechanism to study the soot mass at quasi-steady state (QSS). Their simulation results show that the difference in the total soot mass between different O₂ levels becomes larger as the ambient temperature increases from 850 K to 1200 K under an ambient density of 22.8 kg/m³. Although they predicted similar difference in the soot mass at varying ambient temperatures and O₂ levels as that observed in the experiment [7], detailed explanations on the results, in particular the effects of ambient temperatures and O₂ levels on the soot sub-processes, were not provided in their studies. Setting against this background, the goal of the present study is to elucidate the effects of ambient temperatures and O₂ levels on the global soot formation process as well as on each of the soot sub-processes. To achieve this, LES of Spray A at two different ambient O₂ levels (15% and 21%) and three different ambient temperatures (900 K, 1000 K, and 1100 K) are carried out. The soot is modeled by coupling the LES flow solver with a two-equation soot model that takes the soot sub-processes into account [20].

This article is structured as follows: Descriptions of cases are introduced in Section 2. Numerical methods including LES model, spray model, combustion model and soot model are presented in Section 3. Model validation as well as analysis of soot formation and oxidation across different ambient temperatures and O₂ levels are performed in Section 4. Lastly, concluding remarks are provided in Section 5.

2. Case descriptions

The experimental data from ECN Spray A are used to validate and evaluate the model performance in the present study. Details about the experimental setup and measurement methods are reported in ECN [11]. The main injection parameters of Spray A are described in Table 1. Operating conditions of the simulated cases in the present study are summarized in Table 2. It should be noted that the case with 15% O₂ at the ambient temperature of 900 K (Case 1) is selected as the baseline case.

Table 1
Main injection parameters of Spray A.

Parameters	Value
Injector nozzle diameter	90 μm
Injection pressure	150 MPa
Injection mass flow rate	2.295 g/s
Injection duration	6.1 ms
Fuel temperature	373 K
Fuel density	693 kg/m ³
Liquid spray angle (half)	10°
Discharge coefficient	0.89

Table 2
Main operating conditions of the simulation cases (T_{am} : ambient temperature, ρ_{am} : ambient density).

Case	O ₂ (% mol)	T_{am} (K)	ρ_{am} (kg/m ³)
1	15	900	22.8
2	15	1000	22.8
3	15	1100	22.8
4	21	900	22.8
5	21	1000	22.8
6	21	1100	22.8

3. Numerical methods

In the present study, simulations are carried out using OpenFOAM-v1712 [21], where the Eulerian–Lagrangian approach is used within the LES framework to model fuel spray, gas flow, and combustion processes.

3.1. CFD submodels

The gas-flow field is described in the Eulerian framework using the filtered compressible Navier–Stokes equations [22,23]. To model the sub-grid-scale stress, a one-equation dynamic structure LES model is employed in the present study [23]. For the liquid spray, the standard Lagrangian discrete phase approach is adopted to model the motion of particles. The full geometry of the injector nozzle is not included in the computational domain. Instead, the injector is represented as a ‘disc’ source and is placed at 0.1 mm away from one side of the wall along the wall centroid line. Liquid spray is modeled as Lagrangian parcels, which are injected from the ‘disc’ source. The injection velocity in the simulation is specified as an instantaneous injection velocity with a consideration of cavitation, which can be calculated via $U_f = \dot{m}_f / (C_d \rho_f A_f)$. U_f , \dot{m}_f , C_d , and A_f denote the fuel injection velocity, fuel mass flow rate, discharge coefficient, and orifice exit area, respectively. The fuel mass flow rate is based on a tabulated injection profile recommended by ECN [11]. The aforementioned method to model the injection process is similarly performed by numerous studies [14,24]. In the present study, temperature-dependent fuel properties are considered for the liquid spray parcels. Details of the fuel properties can be seen in Appendix A. The Rosin–Rammler size distribution is considered as the primary breakup of droplets. The Rosin–Rammler parameters are similar to those used in [25,26] where the maximum droplet size is equal to the diameter of the injector nozzle, while the minimum and mean values of the droplet size are set to 10% and 70% of the maximum droplet size, respectively. The detailed parameters for the Rosin–Rammler size distribution are listed in Table 3. The Reitz–Diwakar model is used to model the secondary breakup of droplets [27]. The model constants for the Reitz–Diwakar model are listed in Table 4. Collision between particles is not taken into account due to their minor effects on penetration [28]. Heat transfer between liquid and gas phases is modeled by the Ranz–Marshall correlation [20,29]. In the present LES, the effect of the resolved flow field on the droplets is modeled by the drag force model [30], while the sub-grid turbulence effect on the droplets is accounted for via a sub-grid droplet dispersion model [31].

Table 3
Parameters for the Rosin–Rammner size distribution.

Parameters	Value
Maximum droplet size	90 μm
Minimum droplet size	9 μm
Reference droplet size	63 μm
Exponent	3

Table 4
Model constant for the Reitz–Diwakar model.

Parameters	Value
Bag breakup constant	0.785
Stripping breakup constant	10

3.2. Chemical mechanism and combustion model

In the present study, the reduced $\text{C}_{12}\text{H}_{26}$ mechanism with 54 species and 269 reactions developed by Yao et al. [32] is implemented. The well-stirred reactor is used as the combustion model, in which no sub-grid turbulence chemistry interaction (TCI) effect is considered. To improve the efficiency in integrating the source terms in the species transport and also energy equations, the chemistry coordinate mapping (CCM) approach is employed. A detailed description of CCM can be found in [33–35].

3.3. Soot model

Soot mass fraction (Y_{soot}) and soot particle number density (ϕ_N) are simulated in the current work. The evolution of the two soot transport equations is described by [36,37],

$$\frac{\partial}{\partial t}(\rho Y_{soot}) + \frac{\partial}{\partial x_j}(\rho u_j Y_{soot}) = \frac{\partial}{\partial x_j} \left(\frac{\mu_t}{Sc_t} \frac{\partial Y_{soot}}{\partial x_j} \right) + \frac{dM_{soot}}{dt} \quad (1)$$

$$\frac{\partial}{\partial t}(\rho \phi_N) + \frac{\partial}{\partial x_j}(\rho u_j \phi_N) = \frac{\partial}{\partial x_j} \left(\frac{\mu_t}{Sc_t} \frac{\partial \phi_N}{\partial x_j} \right) + \frac{1}{N_A} \frac{dN_{soot}}{dt} \quad (2)$$

where ρ , u_j , μ_t , and Sc_t denote the fluid density, flow velocity, turbulent viscosity, and turbulent Schmidt number, respectively. The value of Avogadro number (N_A) is $6.022045 \times 10^{26} \text{ kmol}^{-1}$.

The source terms ($\frac{dM_{soot}}{dt}$ and $\frac{dN_{soot}}{dt}$), required in the transported equations, are modeled by a multi-step phenomenological soot model [20]. The source term, $\frac{dM_{soot}}{dt}$, is given as,

$$\frac{dM_{soot}}{dt} = MW_c \left(100\omega_{inc}[\text{C}_2\text{H}_2] + 2\omega_{sg}[\text{C}_2\text{H}_2] - \omega_{OH}[\text{OH}] - \omega_{O_2}[\text{O}_2] \right) \quad (3)$$

where MW_c is the molecular weight of carbon atom. Acetylene (C_2H_2) is selected as the soot precursor and surface growth species. The reaction rates of the sub-processes in terms of inception, surface growth as well as oxidation via OH and O_2 are represented by ω_{inc} , ω_{sg} , ω_{OH} , and ω_{O_2} , respectively. The reaction rate of each sub-process is expressed in an Arrhenius form,

$$\omega_i = C_i T^{b,i} \exp\left(\frac{-T_{a,i}}{T}\right) (S_{soot})^{m,i} \quad (4)$$

$$S_{soot} = (\pi N_{soot})^{1/3} \left(\frac{6M_{soot}}{\rho_{soot}} \right)^{2/3} \quad (5)$$

where T , C , T_a , S_{soot} , and ρ_{soot} denote the gas temperature, model constant, activation temperature, soot specific surface area, and soot density, respectively. b and m are the exponent for T and S_{soot} , respectively. ρ_{soot} is set to 2000 kg/m^3 . The corresponding descriptions and constants for these sub-processes are summarized in Table 5. The

Table 5
Soot model constant values adopted [20].

i	Description	C_i	b	$T_{a,i}$	m
inc	Inception	10000	0	21000	0
sg	Surface growth	$45(p/p_{ref})^{1.4}$	0	12100	0.5
OH	Oxidation by OH	0.36	0.5	0	1.0
O_2	Oxidation by O_2	10000	0.5	19778	1.0

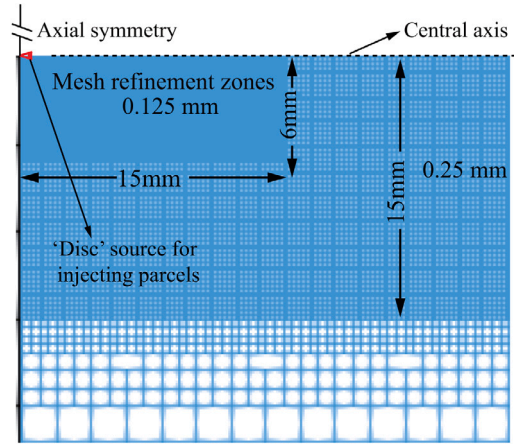


Fig. 1. Mesh configuration of the computational domain. The mesh is axial symmetric. The black dashed line represents the central axis (along with the injection direction) of the computational domain.

surface growth constant (C_{sg}) is adjusted from 14 to 45 [38] in order to match the experimental soot mass provided in the ECN [11].

The source term, $\frac{dN_{soot}}{dt}$, is given as,

$$\frac{dN_{soot}}{dt} = N_A \omega_{inc} - \omega_{coag} \quad (6)$$

$$\omega_{coag} = C_{coag} \left(\frac{24k_B T}{\rho_{soot}} \right)^{1/2} \left(\frac{6M_{soot}}{\rho_{soot}\pi} \right)^{1/6} (N_{soot})^{11/6} \quad (7)$$

where ω_{coag} is the coagulation rate. In Eq. (7), the model constant (C_{coag}) and Boltzmann's constant (k_B) are 3 and $1.38054 \times 10^{-23} \text{ J/K}$, respectively.

3.4. Computational domain and numerical schemes

The computational time step is set to 50 ns. Second-order schemes are used for the discretizations of both time and space. The computational domain, which corresponds to the constant volume vessel in ECN, is a cube with a length of 108 mm for each side. The mesh configuration of the computational domain is shown in Fig. 1. A uniform mesh of 0.25 mm (15 mm axially from the nozzle location) is employed to cover the spray region. A finer mesh of 0.125 mm (6 mm radially and 15 mm axially from the nozzle location) is used to ensure sufficient resolution for the liquid penetration region. In addition, a coarser mesh is employed outside the spray region. The total mesh count is 6.8 million cells. The ratio of the resolved kinetic energy to the total kinetic energy in the spray region is 84%, indicating a sufficient resolution of the flow [39]. A full description of the convergence studies can be found in the authors' previous work [38].

4. Results and discussion

4.1. Validation of non-reacting and reacting spray simulations

The validation of computational model is first carried out by comparing the simulated and measured non-reacting spray characteristics

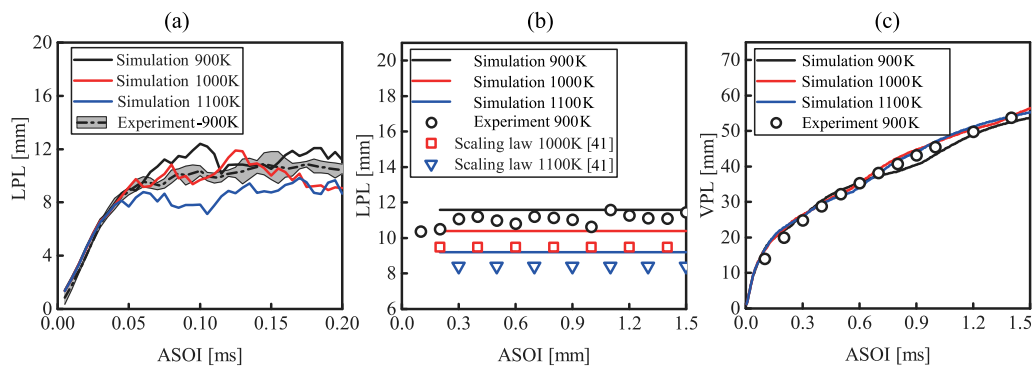


Fig. 2. (a) Liquid penetration length (LPL) during the early stage ($t < 0.2$ ms), (b) LPL during steady state and (c) vapor penetration length (VPL) after the start of injection (ASOI) as function of ambient temperature.

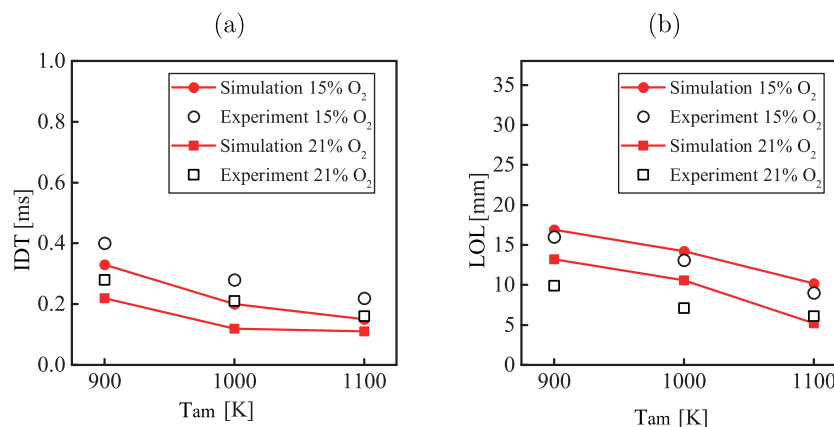


Fig. 3. Simulated and measured (a) ignition delay time (IDT) and (b) lift-off length (LOL) as function of the ambient temperatures (T_{amb}) at 15%, and 21% ambient O_2 [7].

in terms of liquid penetration length (LPL) and vapor penetration length (VPL). In this study, the LPL and VPL, as recommended in ECN [11,40], are defined as the farthest distance where 95% of the total liquid mass and 0.1% of the vapor fuel mass are observed, respectively. Fig. 2(a) shows the temporal evolution of LOL during the early phases of injection ($t < 0.2$ ms), in which the present model is shown to be able to capture the fuel evaporation process. As shown in Fig. 2(b), the measured LPL at the ambient temperature of 900 K is used to validate the associated prediction during the QSS. Considering that the LPL measurements at the ambient temperature of 1000 K and 1100 K are not available, the LPLs obtained from the scaling law are hence used to validate the predicted LPLs [41]. It should be noted that the measured LPL at the ambient temperature of 900 K is ensemble averaged based on different individual injection events, while the simulated LPLs at different ambient temperatures are time averaged from 0.2 ms to 1.5 ms. As shown in Fig. 2(b), although the predicted LPLs are overpredicted as compared to those obtained from the experiment at the ambient temperature of 900 K and the scaling law at the ambient temperature of 1000 K and 1100 K [41], the maximum relative error is within 9%. The same overpredictions can also be found in [23,24,26]. Nevertheless, the overall trend where LPLs decrease as the ambient temperature increases is well captured. Further information regarding the sensitivity of the LPL to the stripping breakup constant (C_s) in the Reitz–Diwakar model is shown in Appendix B. Considering that the ambient temperature has a minor effect on the VPL [42], the predicted VPLs at different ambient temperatures are only compared to the measurement at the ambient temperature of 900 K. Fig. 2(c) demonstrates that the predicted VPLs at varying ambient temperatures are in good agreement with the measurement.

The LES reacting spray characteristics are validated using the experimental ignition delay time (IDT) and lift-off length (LOL). In the

present study, the predicted IDT is defined as the time when the maximum rate of change in maximum temperature in the domain is observed [43]. This definition is in accordance to the definition of experimental IDT recommended by ECN [11] and has been used in various studies [9,24,44]. The predicted LOL, based on ECN's recommendation [11,45], is defined as the shortest downstream location where the mass fraction of OH reaches 2% of its maximum value after the spray flame stabilizes. The measured and predicted IDTs are shown in Fig. 3(a) where the predicted IDTs follow the trend of measured IDTs [7], but are consistently underpredicted. The underestimation is likely due to the reduced mechanism used as similar underestimation of IDTs can also be found in [46,47], in which the same reduced chemical mechanism was employed. To examine the influence of C_s on IDT, a sensitive study of C_s on IDT is shown in Appendix B. The current LES captures the variation of LOLs with respect to the change of ambient temperatures. This is shown in Fig. 3(b), where the predicted LOLs agree well with the measured LOLs [7], except for the 21% O_2 cases at the ambient temperature of 900 K and 1000 K. The overpredictions of LOLs for these two cases are likely due to the uncertainties in the experiment. In another experimental work using the Sandia bomb with 21% O_2 , the measured LOLs were reported to be 13.2 mm and 10.1 mm at the ambient temperature of 900 K and 1000 K [48], respectively. The present simulated LOLs for these two cases are 13.3 mm and 10.6 mm, respectively, which leads to a maximum relative error of 5% as compared to the experimental data in [48].

4.2. Transient soot evolution and quasi-steady soot mass

The model performance in predicting the transient evolution of the total soot mass in the baseline case (ambient temperature and O_2 level of 900 K and 15%, respectively) is assessed. Fig. 4 shows

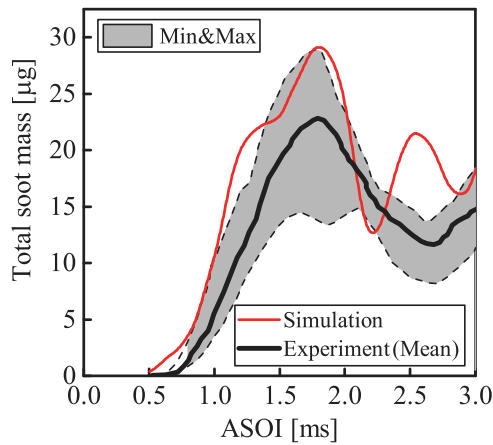


Fig. 4. Comparison of the simulated and measured soot mass evolution after the start of injection (ASOI) for the baseline case (900 K, 15% O₂).

a comparison of the measured and predicted temporal evolutions of the total soot mass in the baseline case. In the experiment, only the soot within the region from the injector nozzle to 67.2 mm downstream location is measured [11]. Akin to the practice in the experiment, only the simulated soot in the aforementioned region is considered in the total soot mass calculation. It should be noted that the mean value of the measured soot mass is ensemble averaged from at least 5 individual injection events of which the associated scatter of soot mass in the 5 experimental injection events is shown as the shadow region in Fig. 4. As shown in Fig. 4, both the predicted and measured soot mass increase rapidly and then decrease before reaching the QSS. This phenomenon is referred to soot spike and is well captured by the present LES model. Extensive discussion on the soot spike is available in the authors' previous study [38]. Further discussion regarding the variation of soot spike with the different ambient temperatures and O₂ levels are beyond the scope of the present work, and hence is presented in Appendix C. This rapid raise of the soot mass is similarly observed under different ambient O₂ levels and temperatures (cases 2 to 6). Fig. 5 compares the distributions of the simulated SVF and measured soot optical thickness (KL) [11] at three different time instances (1.0 ms, 1.4 ms, and 2.5 ms) in the baseline case (900 K, 15% O₂). As depicted in Fig. 5, although the simulated SVF penetrates slightly shorter than

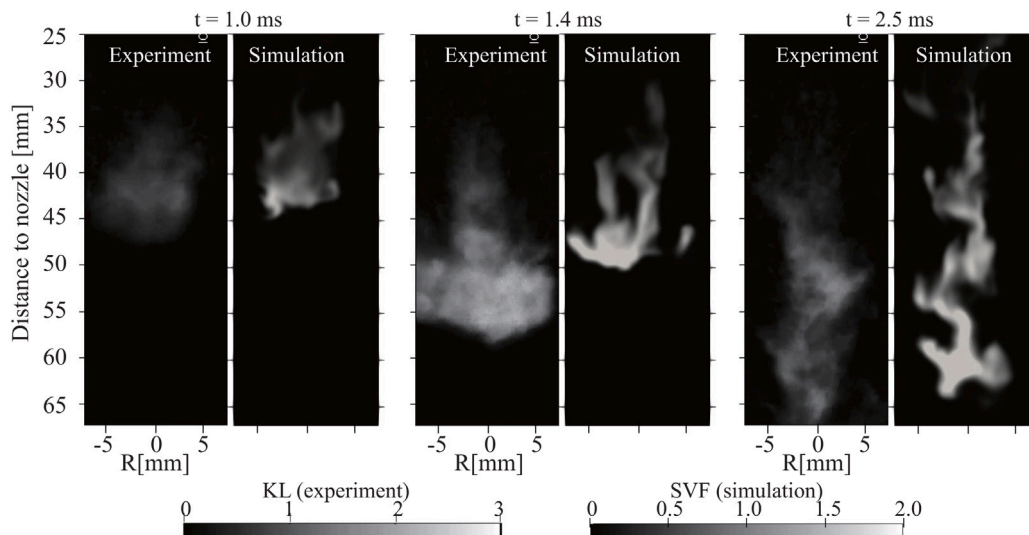


Fig. 5. Comparison of the distributions of the simulated soot volume fraction (SVF) and measured soot optical thickness (KL) [11] after the start of injection (ASOI) for the baseline case (900 K, 15% O₂) [11].

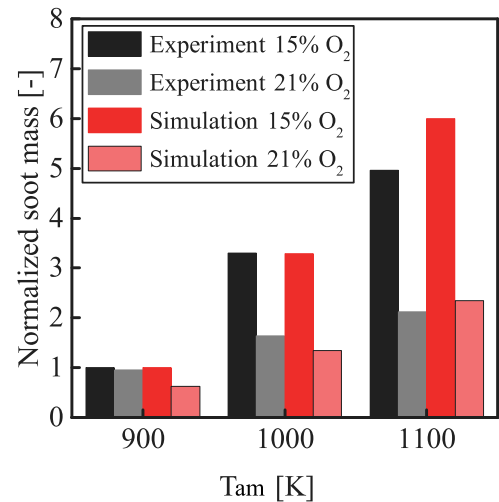


Fig. 6. Comparison of simulated and measured quasi-steady soot mass for all cases. The simulated results are time averaged from 2.0 to 4.0 ms, while the experimental results are time and ensemble averaged within 4.0 ms from 5 individual injection events [7].

the measured soot KL, the evolution of soot-containing regions in the simulated SVF is well captured.

To further validate the model performance at QSS across different ambient temperatures and O₂ levels, a comparison of the simulated and measured soot mass [11] at the QSS is presented in Fig. 6, where the simulated soot mass is time averaged from 2.0 to 4.0 ms. It should be noted that both the measured and simulated soot mass are normalized by their respective soot mass under the baseline conditions (900 K, 15% O₂). Fig. 6 depicts that the normalized simulated soot mass agrees well with the normalized measured soot mass. It can be found that the soot mass increases with increasing ambient temperature, but decreases as the ambient O₂ level increases from 15% to 21%. It is also worth noting that the difference in the soot mass between the 15% and 21% O₂ cases becomes larger as the ambient temperature increases. Above all, the variation of the soot mass with respect to the change of ambient O₂ levels and temperatures is consistent with that observed in the experiment [7].

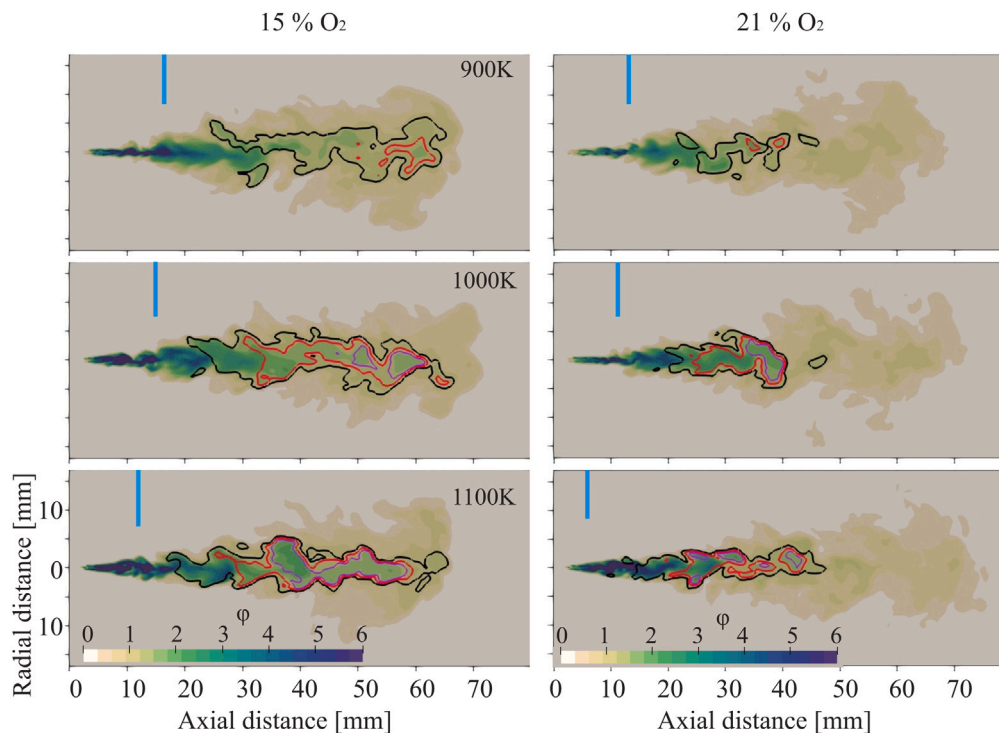


Fig. 7. Instantaneous distribution of equivalence ratio (ϕ) in a cut plane for different ambient temperatures and O_2 levels at 2.5 ms. Black, red and purple lines are iso-line of soot volume fraction = 10^{-6} , 2×10^{-5} and 3×10^{-5} , respectively. The short cyan vertical lines denote the simulated lift-off lengths.

4.3. Effects of ambient temperatures and O_2 levels on global soot process

Considering that the soot formation is highly related to local mixture fraction [17], Fig. 7 shows the instantaneous distribution of equivalence ratio (ϕ) at 2.5 ms for different ambient temperatures and O_2 levels. It is apparent that the soot-containing region in the 15% O_2 cases is larger than that in the 21% O_2 cases. This corresponds to a higher soot mass observed in the 15% O_2 cases, as shown in Fig. 6. The soot onset appears more upstream due to the shorter LOL as the ambient temperature increases. The soot is mainly formed up till the 50 mm downstream location in the 21% O_2 cases, while it is formed up till the head of spray in the 15% O_2 cases. The reason can be attributed to the fact that the fuel-rich region penetrates to further downstream location in the 15% O_2 cases. In order to demonstrate the local difference in ϕ between different cases, Fig. 8 shows the scatter plots of $\phi - T$ at different ambient temperatures and O_2 levels. It should be noted that the soot region extends to a higher value of ϕ in both the 15% and 21% O_2 cases as the ambient temperature increases. Considering that the flame stabilization is established at QSS, only the mean flame temperature profiles at 2.5 ms as a function of ϕ at different ambient temperatures in the 15% and 21% O_2 cases are shown in Fig. 9. As depicted, the O_2 level has a more significant effect on the maximum flame temperature than the ambient temperature. The mean flame temperature in the case with a higher ambient temperature is higher in both the 15% and 21% O_2 cases. It is known that a higher flame temperature leads to faster reaction rates for both formation and oxidation rates based on Arrhenius relation. However, an increasing flame temperature in the relatively fuel-rich mixture results in a faster soot formation than oxidation due to a lack of significant oxidative attack on the soot precursor, as reported in [43,49,50]. This is the governing factor which leads to the increase in the soot mass with increasing ambient temperature cf. Fig. 6.

As aforementioned, the soot mass difference at 15% and 21% O_2 becomes larger when the ambient temperature increases. In order to understand the mechanism behind this increasing difference in the soot mass with increasing ambient temperature, the mass distributions of

soot and soot precursor (C_2H_2 selected as the soot precursor and surface growth species) conditional on ϕ at different ambient temperatures and O_2 levels are shown in Fig. 10. The following observations in Fig. 10 are similar during the QSS (2.0 to 4.0 ms), only the results at 2.5 ms are hence shown here. From Fig. 10(a), the soot mass in the 15% O_2 cases is higher than that in the 21% O_2 cases, which corresponds to the observation in Fig. 6. It is also obvious from Fig. 10(a) that the distribution of soot is extended to a higher ϕ value as the ambient temperature increases. This agrees well with the spatial soot distribution shown in Fig. 7. More importantly, the amount of soot formed in the fuel-rich region (roughly $\phi > 1.6$) is found to increase with increasing ambient temperature. This is more apparent in the 15% O_2 cases. As a result, the difference in the soot mass appears in a wider range of ϕ and increases between the 15% and 21% O_2 cases with the rise of ambient temperature. These observations may be attributed to the C_2H_2 formed as a similar distribution is observed in Fig. 10(b).

An examination of C_2H_2 reaction pathways (not shown here) indicates that the two most important pathways to affect C_2H_2 production are $C_2H_2 + O \leftrightarrow CO + CH_2$ and $C_2H_2 + OH \leftrightarrow CO + CH_3$. Meanwhile, it is expected that the productions of O and OH radicals decrease as the O_2 level decreases. Hence, it is suggested that the lower amount of C_2H_2 formed in the 21% O_2 cases is due to a stronger oxidation process via O and OH radicals, as compared to that in the 15% O_2 cases. However, a lower C_2H_2 may not be the only governing reason for the lower soot mass in the 21% O_2 cases. Since a higher amount of OH produced in the 21% O_2 cases cf. Fig. 15(a), another important reason for the lower soot mass observed at 21% O_2 is found to be the stronger soot oxidation rate via OH as compared to 15% O_2 cases. When the ambient temperature increases, the flame temperature also increases as shown in Fig. 9. This results in the relatively high ϕ region becoming favorable for the formation of C_2H_2 . Within the relatively high ϕ region, the oxidation of C_2H_2 is not significant. Hence, more C_2H_2 is formed at the relatively high ϕ region, which also leads to the soot formed at that particular region. In addition to this, the LOL decreases as the ambient temperature increases cf. Fig. 3(b). This results in a larger fuel-rich region due to a shorter mixing time between air and fuel.

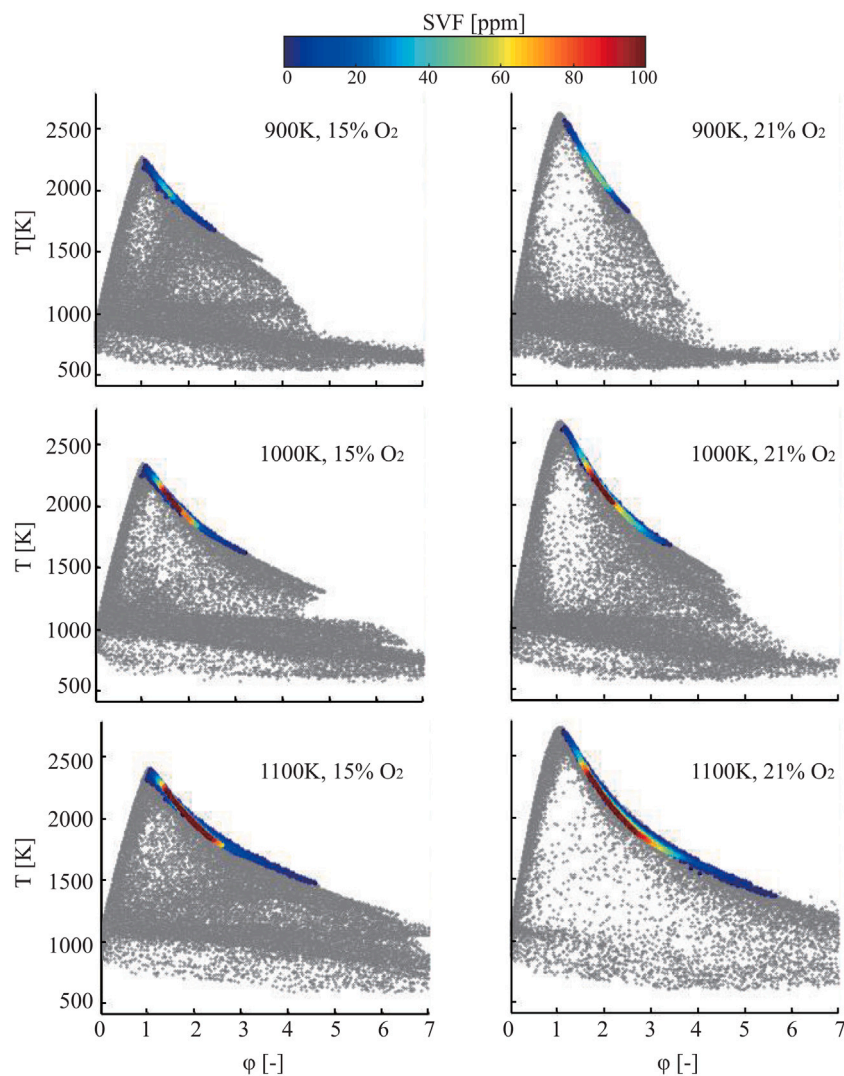


Fig. 8. Scatter plots of equivalence ratio-temperature ($\phi-T$) at different ambient temperatures and oxygen levels. Gray dots represent all computational cells. Colorful dots denote the cells with soot volume fraction (SVF) larger than 1 ppm (particle per million), which envelops the high SVF region.

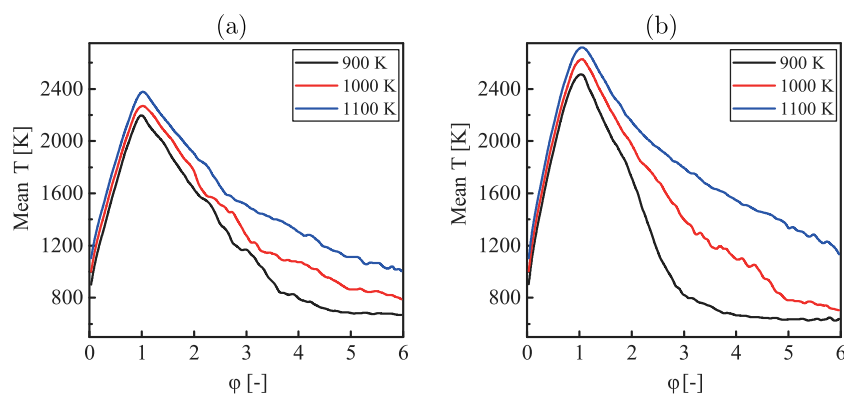


Fig. 9. Mean temperature conditional on equivalence ratio (ϕ) at 2.5 ms for different ambient temperatures under (a) 15% and (b) 21% O_2 levels.

All these collectively lead to the increase of soot mass as the ambient temperature increases. This is more apparent in the 15% O_2 cases due to having a weaker oxidation of C_2H_2 as compared to the 21% O_2 cases. It is also worth noting that the relatively high ϕ region is the most favorable region for soot formation cf. Fig. 7. As a result, the formation of C_2H_2 , especially in the relatively high ϕ region, increases more drastically at 15% O_2 than at 21% O_2 . This, consequently, leads

to an increasing difference in soot mass formed between the 15% and 21% O_2 cases as the ambient temperature increases.

A closer examination of Fig. 10(a) shows that soot is formed closer to the stoichiometric line ($\phi = 1$) in the 15% O_2 cases. The main reason is likely due to the presence of C_2H_2 at the region near stoichiometric mixture, as shown in Fig. 10(b). As mentioned earlier, the oxidation of C_2H_2 is mainly via O and OH radicals. Fig. 11 shows the mass

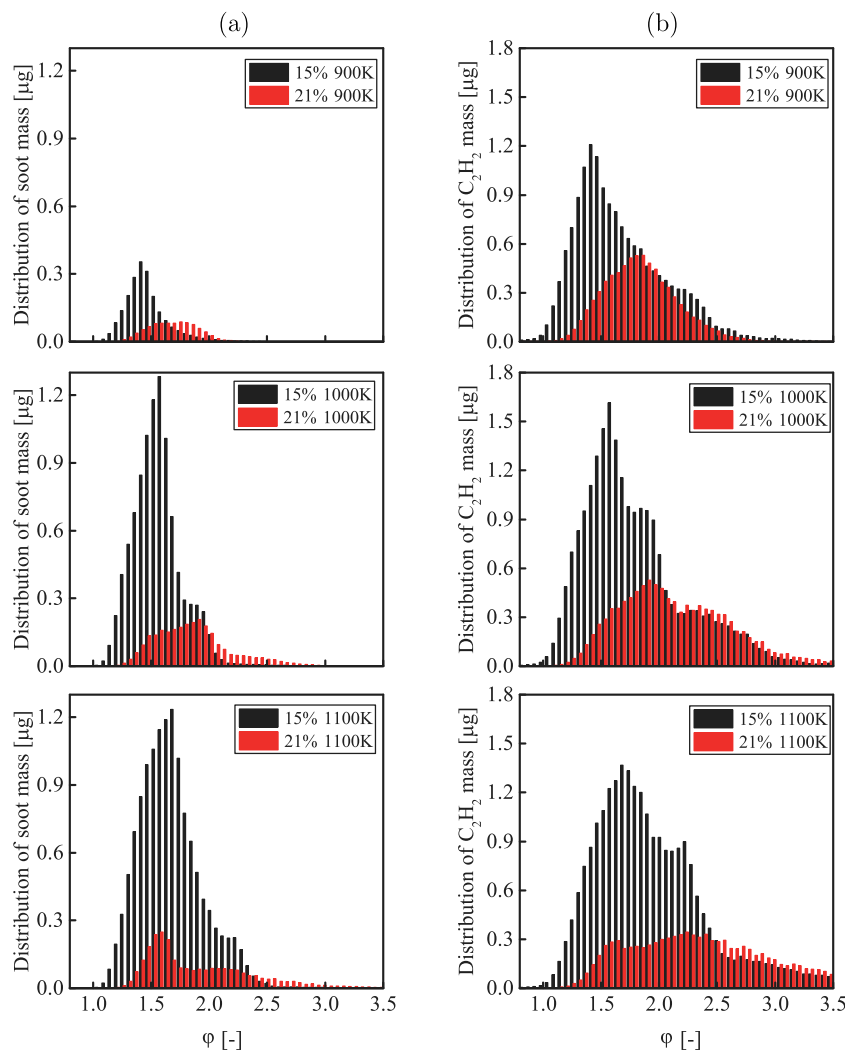


Fig. 10. Distributions of (a) soot and (b) C_2H_2 mass as a function of equivalence ratio (ϕ) for different ambient temperatures and O_2 levels at 2.5 ms.

distributions of O and OH radicals as a function of ϕ at 2.5 ms. It is apparent that the O and OH radicals mass in the 21% O_2 cases are greater than that in the 15% O_2 cases. This demonstrates that the C_2H_2 oxidation near the stoichiometric region in the 21% O_2 cases is significantly stronger than that in the 15% O_2 cases. This likely leads to more C_2H_2 being consumed in the 21% O_2 cases relative to the 15% O_2 cases. Hence, C_2H_2 can be observed closer to the stoichiometric region in the 15% O_2 cases, as compared to that in the 21% O_2 cases.

4.4. Effects of ambient temperatures and O_2 levels on soot sub-processes

In this section, the effects of ambient temperatures and O_2 levels on each soot sub-processes are investigated. Fig. 12 shows the temporal evolution of the soot mass contributed by the inception (M_{inc}) and surface growth processes (M_{sg}) across different ambient temperatures and O_2 levels. It is apparent that both M_{inc} and M_{sg} increase with increasing ambient temperature at both 15% and 21% O_2 levels. This may be attributed to the higher amount of C_2H_2 formed and increasing flame temperature when the ambient temperature increases [50]. During the inception process, M_{inc} in the 21% O_2 cases is always higher than that in the 15% O_2 cases. Although the C_2H_2 mass in the 21% O_2 cases is lower than that in the 15% O_2 cases, the local flame temperature in the 21% O_2 cases is higher than that in the 15% O_2 cases. This higher flame temperature results in a higher inception rates in the 21% O_2 cases. It should be noted that the surface growth process is more

dominant than the inception process as M_{inc} is lower than M_{sg} by an order of magnitude of 100. During the surface growth process, M_{sg} in the 15% O_2 cases is always lower than that in the 21% O_2 cases at the ambient temperature of 900 K. For the ambient temperatures of 1000 K and 1100 K, M_{sg} in the 15% O_2 cases is lower at the beginning but overtakes that in the 21% O_2 cases during the QSS. It is worth noting that the soot sub-process rates are highly dependent on the concentration of soot-related species, soot surface area, and local flame temperature (see Eq. (3)). Fig. 13 shows the evolution of soot surface area across different ambient temperatures and O_2 levels. It is apparent that the soot surface area in the 15% O_2 cases is smaller than that in the 21% O_2 cases at the early stage, but larger during the QSS. At the ambient temperature of 900 K, M_{sg} in the 15% O_2 cases is lower due to the lower flame temperature cf. Fig. 9. At the ambient temperature of 1000 K and 1100 K, the earlier soot onset and higher local flame temperature in the 21% O_2 cases result in a higher M_{sg} at the early time. However, as the flame develops, the soot surface area in the 15% O_2 cases becomes larger than that in the 21% O_2 cases cf. Fig. 13. Hence, the larger soot surface area and higher C_2H_2 mass cause the M_{sg} in the 15% O_2 cases to be higher than that in the 21% O_2 cases during the QSS. Fig. 14 shows the temporal evolution of soot mass oxidized via OH and O_2 (M_{OH} and M_{O_2}) across different ambient temperatures and O_2 levels. It is noticeable that the M_{OH} and M_{O_2} increase with increasing ambient temperature in both the 15% and 21% O_2 cases. Fig. 14 also shows that the soot mass oxidized via OH in the 21%

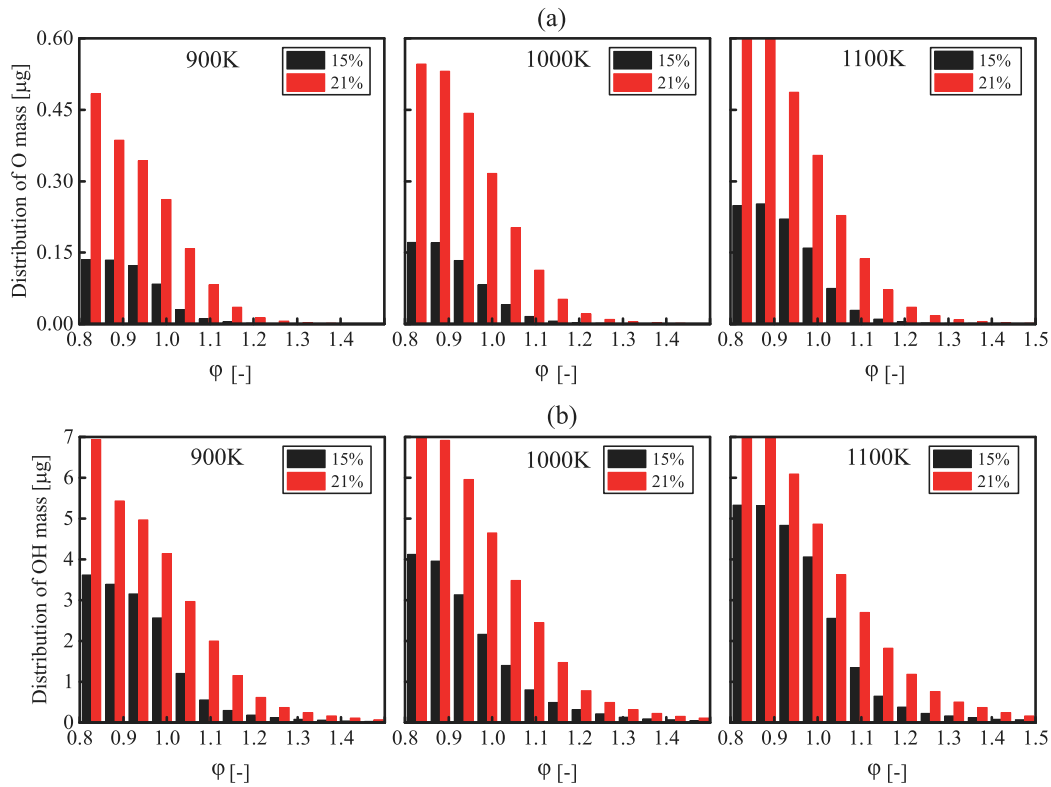


Fig. 11. Distributions of (a) O and (b) OH radicals mass as a function of equivalence ratio (φ) for different ambient temperatures and O_2 levels at 2.5 ms.

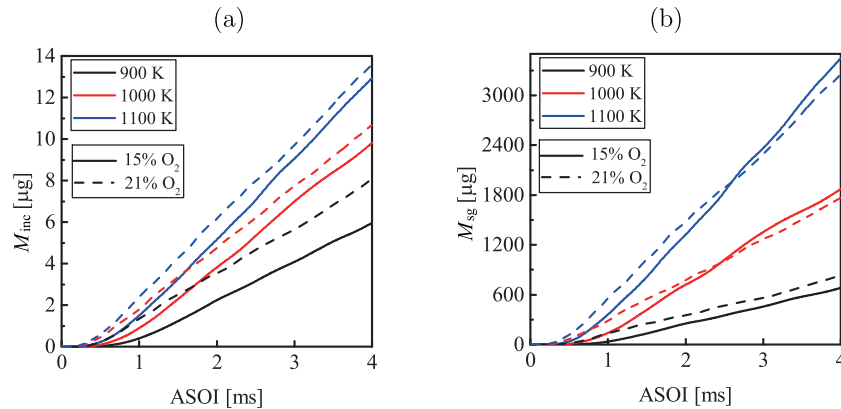


Fig. 12. The temporal evolution of soot mass resulted from (a) inception (M_{inc}) and (b) surface growth (M_{sg}) after the start of injection (ASOI) across different ambient temperatures and O_2 levels.

O_2 cases is consistently higher than those in the 15% O_2 cases during the entire soot evolution process for all three ambient temperatures. On the contrary, the M_{O_2} values in the 21% O_2 case are higher than those in the 15% O_2 case at the early time but become lower during the QSS. To better understand the observed results, Fig. 15 shows the total mass of OH and O_2 across different ambient temperatures and O_2 levels. As depicted, the OH mass in the 21% O_2 cases is higher than that in the 15% O_2 cases. Despite having smaller soot surface area, the significantly higher flame temperature and OH concentration at 21% O_2 are the main reason for M_{OH} to be consistently higher relative to that at 15% O_2 . Fig. 15(b) shows the remained O_2 mass for the spray region in the 21% and 15% O_2 cases at different ambient temperatures. The mixture fraction $Z = 0.0001$ is used as a threshold to define the boundary of the spray region. From Fig. 15(b), there is no difference in the remained O_2 mass for the spray region between the 15% and 21% O_2 cases. Hence, the difference in the M_{O_2} can be attributed to

the soot surface area and flame temperature. At the early phase, the higher flame temperature and earlier soot onset in the 21% O_2 cases lead to a higher M_{O_2} . However, the soot surface area in the 15% O_2 cases becomes significantly larger during the QSS. This causes M_{O_2} to become larger than that in the 21% O_2 cases.

5. Conclusions

In this study, the soot formation and oxidation processes are investigated using large eddy simulation across different ambient temperatures (900 K, 900 K, and 1100 K) and oxygen (O_2) levels (15% and 21%). The predicted relative change of time-averaged soot mass during the quasi-steady state agrees well with the experimental measurements.

A lower soot precursor (C_2H_2) mass is formed in the 21% O_2 cases due to a stronger oxidation of C_2H_2 via O and OH radicals, as compared to the 15% O_2 cases. This leads to a lower soot mass formed in the

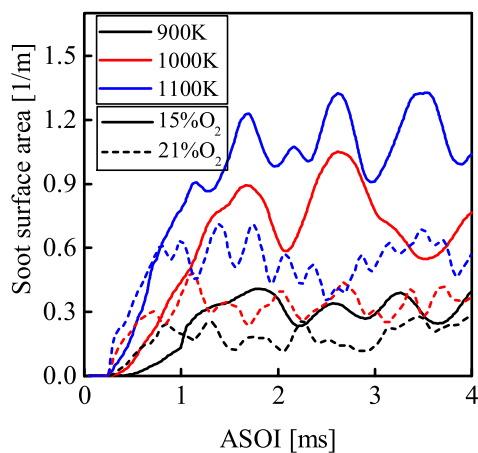


Fig. 13. The temporal evolution of soot surface area after the start of injection (ASOI) across different ambient temperatures and O_2 levels.

21% O_2 cases. The increase in the ambient temperature causes the fuel-richer region (equivalence ratio > 1.6) to be favorable for C_2H_2 formation, and consequently, soot to form. The effects of temperature are more significant in the 15% O_2 cases due to a lower amount of O and OH radicals produced, which leads to a weaker oxidation of C_2H_2 . This eventually results in a significantly larger amount of C_2H_2 formed at 15% O_2 than 21% O_2 as the ambient temperature rises. Consequently, the difference in the soot mass formed between the 15 and 21% O_2 cases becomes larger as the ambient temperature increases.

At the ambient temperature of 900 K, a higher local flame temperature in the 21% O_2 case leads to a higher soot mass resulted from surface growth process. At the ambient temperature of 1000 K and 1100 K, an earlier soot onset and higher local flame temperature lead to a higher surface growth mass in the 21% O_2 cases at the early time. However, during the quasi-steady state, the soot surface area in the 15% O_2 cases becomes larger than that in the 21% O_2 cases, which leads to the surface growth mass in the 15% O_2 cases to become higher. The soot mass oxidized via OH in the 21% O_2 cases is consistently higher than that at 15% O_2 cases due to the significantly higher OH mass and flame temperatures present in the former cases. On the other hand, the difference in soot oxidation process via O_2 mainly results from the difference in soot surface area and flame temperatures in the 15% O_2 and 21% O_2 cases.

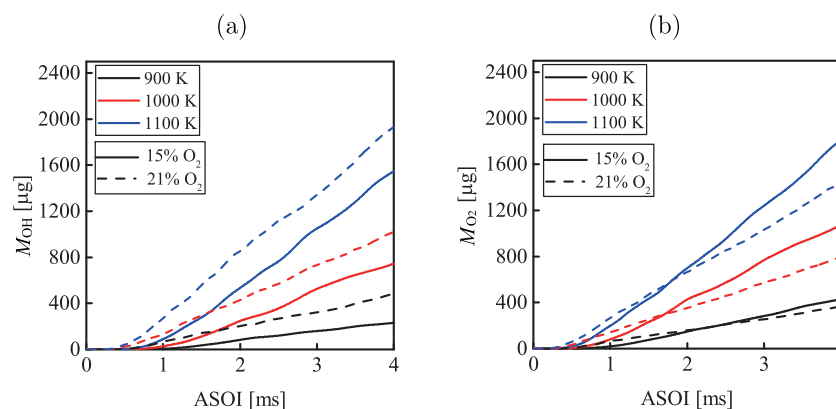


Fig. 14. The evolution of soot mass resulted from (a) OH oxidation (M_{OH}) and (b) O_2 oxidation (M_{O_2}) after the start of injection (ASOI) across different ambient temperatures and O_2 levels.

CRediT authorship contribution statement

Min Zhang: Conceptualization, Methodology, Validation, Writing – original draft. **Jiun Cai Ong:** Methodology, Supervision, Writing – review. **Kar Mun Pang:** Conceptualization, Supervision, Writing – review & editing. **Xue-Song Bai:** Supervision, Writing – review. **Jens H. Walther:** Supervision, Writing – review & editing.

Declaration of competing interest

The authors declare that they have no known competing financial interests or personal relationships that could have appeared to influence the work reported in this paper.

Acknowledgments

Min Zhang was sponsored by China Scholarship Council (CSC). Jiun Cai Ong gratefully acknowledged the financial support from the Independent Research Fund Denmark (DFF) and MAN Energy Solutions under the grant number 8022-00143B. The computation was performed using Niflheim cluster at Technical University of Denmark (DTU). The authors acknowledged PRACE for awarding us access to Joliot-Curie at GENCI@CEA, France.

Appendix A. Modeled fuel properties

Fig. A.1 shows a comparison of modeled fuel parameters in OpenFOAM and experimental data from National Institute of Standards and Technology, US (NIST) [51]. The main fuel physical properties to affect LPL are surface tension, liquid dynamic viscosity, and fuel density. It is apparent that the fuel physical properties are well modeled in the present study.

Appendix B. Sensitive study of C_s on LPL and IDT

The breakup model constant, stripping breakup constant (C_s) in the Reitz–Diwakar model, is the common tuning parameter to vary LPL [52,53]. Fig. B.1 show the evolution of LPLs with respect to different C_s values at the ambient temperature of 900 K and 0% O_2 , respectively. As depicted, it is apparent that the LPL is insensitive to the C_s value in the present LES model.

Table B.1 shows the IDT with respect to different C_s at the ambient temperature of 900 K and 15% O_2 . From Table B.1, the IDT is shown to be insensitive to the C_s value. Considering that $C_s = 10$ is the default value in OpenFOAM, the default value is used in the secondary breakup model for the present study.

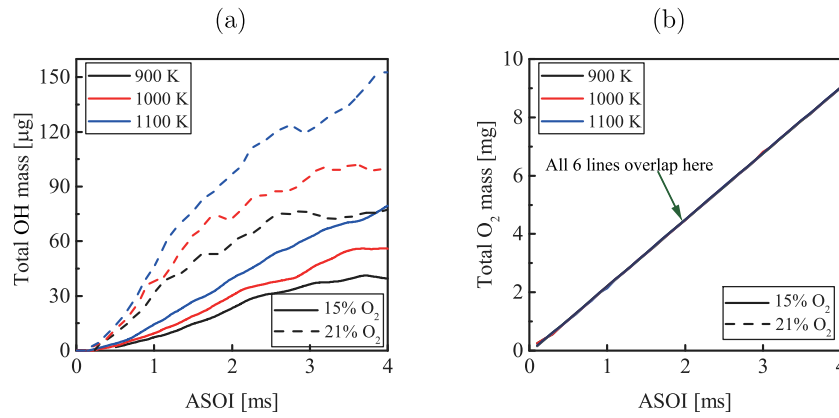


Fig. 15. The temporal evolution of (a) total OH mass and (b) total O₂ mass in the spray region after the start of injection (ASOI) between 21% and 15% O₂ levels at different ambient temperatures.

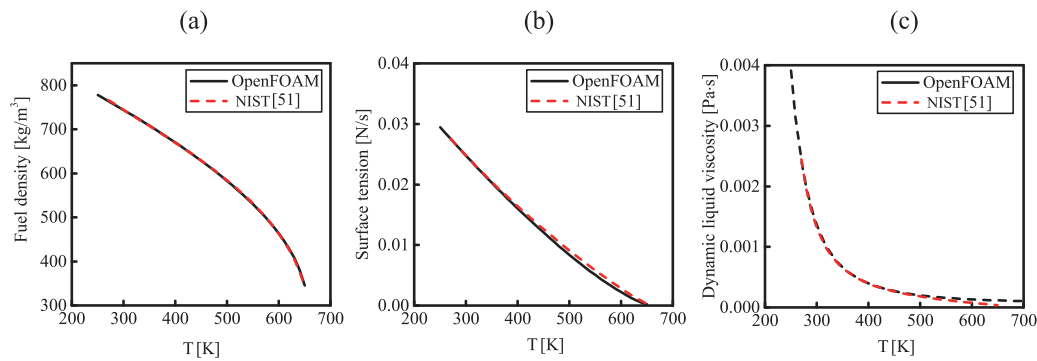


Fig. A.1. Comparison of fuel properties for (a) fuel density, (b) surface tension, and (c) dynamic liquid viscosity between modeling results and results from [51].

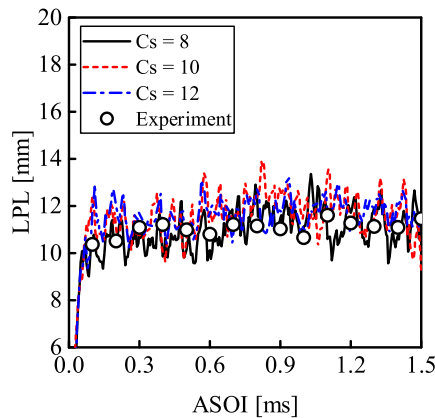


Fig. B.1. Comparison of LPLs between different C_s values. The experiment data is from ECN [11].

Table B.1
IDTs for different C_s values at the ambient temperature of 900 K and 15% O₂.

	Experiment [11]	$C_s = 10$ (Present)	$C_s = 8$	$C_s = 12$
IDT (ms)	0.40	0.33	0.33	0.32

Appendix C. Soot spike at different ambient temperatures and O₂ levels

A detailed explanation on the formation of soot spike was provided in the authors' previous work [38] for different oxygen levels at the ambient temperature of 900 K. As discussed in [38], the oxidation

process becomes more dominant than the formation process due to the continually increasing OH radicals. This leads to a decrease in the total soot mass and, hence the formation of soot spike.

Experimental studies from ECN [11] have shown that the soot spike becomes less obvious as ambient temperature increases at a fixed oxygen level of 15%. As mentioned in Section 4.3, when the ambient temperature increases, the increasing flame temperature results in the soot formation process increasing faster than the soot oxidation process. This causes the oxidation process to be less dominant at high ambient temperatures, even though OH radicals continue to increase. As a consequence, a less significant soot spike is observed as the ambient temperature increases.

References

- [1] Idicheri CA, Pickett LM. Soot formation in diesel combustion under high-EGR conditions. SAE Trans 2005;114:1559–74.
- [2] Farrace D, Bolla M, Wright YM, Boulouchos K. Numerical study of the influence of EGR on in-cylinder soot characteristics in a heavy-duty diesel engine using CMC. SAE Trans 2014;7:256–68.
- [3] Agarwal AK, Singh AP, Maurya RK. Evolution, challenges and path forward for low temperature combustion engines. Prog Energy Combust Sci 2017;61:1–56.
- [4] Tree DR, Svensson KI. Soot processes in compression ignition engines. Prog Energy Combust Sci 2007;33:272–309.
- [5] Polonowski CJ, Mueller CJ, Gehrke CR, Bazyn T, Martin GC, Lillo PM. An experimental investigation of low-soot and soot-free combustion strategies in a heavy-duty, single-cylinder, direct-injection, optical diesel engine. SAE Int J Fuels Lubr 2012;5:51–77.
- [6] Gallo Y, Malmberg VB, Simonsson J, Svensson E, Shen M, Bengtsson P-E, Pagels J, Tunér M, Garcia A, Andersson Ö. Investigation of late-cycle soot oxidation using laser extinction and in-cylinder gas sampling at varying inlet oxygen concentrations in diesel engines. Fuel 2017;193:308–14.
- [7] Skeen SA, Manin J, Dalen K, Pickett LM. Extinction-based imaging of soot processes over a range of diesel operating conditions. In: 8th us national combustion meeting 2013. Utah, USA: Western States Section/Combustion Institute; 2013, p. 1981–93.

- [8] Cenker E, Bruneaux G, Pickett L, Schulz C. Study of soot formation and oxidation in the engine combustion network (ECN), spray A: Effects of ambient temperature and oxygen concentration. *SAE Int J Engines* 2013;5(1):352–62.
- [9] Pei Y, Hawkes ER, Bolla M, Kook S, Goldin GM, Yang Y, Pope SB, Som S. An analysis of the structure of an n-dodecane spray flame using TPDF modelling. *Combust Flame* 2016;168:420–35.
- [10] Shen M, Malmborg V, Gallo Y, Waldheim BB, Nilsson P, Eriksson A, Pagels J, Andersson O, Johansson B. Analysis of soot particles in the cylinder of a heavy duty diesel engine with high egr. *SAE Trans* 2015.
- [11] Engine Combustion Network, 0000. available from: <https://ecn.sandia.gov/ecn-data-search/>.
- [12] Siebers DL. Liquid-phase fuel penetration in diesel sprays. *SAE Trans* 1998;1205–27.
- [13] Pei Y, Hu B, Som S. Large-eddy simulation of an n-dodecane spray flame under different ambient oxygen conditions. *J Energy Res Technol* 2016;138(3).
- [14] Mukut KM, Roy SP. Effect of O₂ concentration in ambient mixture and multi-phase radiation on pollutant formation in ECN spray A. *Combust Theor Model* 2020;24:549–72.
- [15] Aubagnac-Karkar D, Michel J-B, Colin O, Darabiha N. Combustion and soot modelling of a high-pressure and high-temperature dodecane spray. *Int J Engine Res* 2018;19(4):434–48.
- [16] Lucchini T, Pontoni D, D'Errico G, Somers B. Modeling diesel combustion with tabulated kinetics and different flame structure assumptions based on flamelet approach. *Int J Engine Res* 2020;21:89–100.
- [17] Gong C, Jangi M, Bai XS. Large eddy simulation of n-dodecane spray combustion in a high pressure combustion vessel. *Appl Energy* 2014;136:373–81.
- [18] Pandurangi SS, Bolla M, Wright YM, Boulouchos K, Skeen SA, Manin J, Pickett LM. Onset and progression of soot in high-pressure n-dodecane sprays under diesel engine conditions. *Int J Engine Res* 2017;18:436–52.
- [19] Wang H, Ra Y, Jia M, Reitz RD. Development of a reduced n-dodecane-PAH mechanism and its application for n-dodecane soot predictions. *Fuel* 2014;136:26–36.
- [20] Pang KM, Jangi M, Bai X-S, Schramm J. Evaluation and optimization of phenomenological multi-step soot model for spray combustion under diesel engine-like operating conditions. *Combust Theor Model* 2015;19(3):279–308.
- [21] Weller HG, Tabor G, Jasak H, Fureby C. A tensorial approach to computational continuum mechanics using object-oriented techniques. *Comput Phys* 1998;12:620–31.
- [22] Liu K, Haworth DC, Yang X, Gopalakrishnan V. Large-eddy simulation of motored flow in a two-valve piston engine: POD analysis and cycle-to-cycle variations. *Flow Turbul Combust* 2013;91(2):1–31.
- [23] Senecal PK, Pomraning E, Richards KJ, Som S. An investigation of grid convergence for spray simulations using an les turbulence model. *SAE technical paper* 01-1083, 2013.
- [24] Kahila H, Wehrfritz A, Kaario O, Masouleh MG, Maes N, Somers B, Vuorinen V. Large-eddy simulation on the influence of injection pressure in reacting spray A. *Combust Flame* 2018;191:142–59.
- [25] D'Errico G, Lucchini T, Contino F, Jangi M, Bai X-S. Comparison of well-mixed and multiple representative interactive flamelet approaches for diesel spray combustion modelling. *Combust Theor Model* 2014;18(1):65–88.
- [26] Desantes JM, García-Oliver JM, Novella R, Pérez-Sánchez EJ. Application of a flamelet-based CFD combustion model to the LES simulation of a diesel-like reacting spray. *Comput & Fluids* 2020;200.
- [27] Reitz RD, Diwakar R. Effect of drop breakup on fuel sprays. *SAE tech. paper ser.* 860469, 1986, p. 1–10.
- [28] Jangi M, D'Errico G, Bai X-S, Lucchini T. Numerical simulation of the ecn spray a using multidimensional chemistry coordinate mapping: n-dodecane diesel combustion. *SAE technical paper* 01-1660, 2012.
- [29] Chishty MA, Bolla M, Hawkes ER, Pei Y, Kook S. Soot formation modelling for n-dodecane sprays using the transported PDF model. *Combust Flame* 2018;192:101–19.
- [30] Liu AB, Mather D, Reitz RD. Modeling the effects of drop drag and breakup on fuel sprays. *SAE Trans* 1993;83–95.
- [31] Bharadwaj N, Rutland CJ. A large-eddy simulation study of sub-grid two-phase interaction in particle-laden flows and diesel engine sprays. *At Sprays* 2010;20.
- [32] Yao T, Pei Y, Zhong B-J, Som S, Lu T, Luo KH. A compact skeletal mechanism for n-dodecane with optimized semi-global low-temperature chemistry for diesel engine simulations. *Fuel* 2017;191:339–49.
- [33] Jangi M, Yu R, Bai X-S. Development of chemistry coordinate mapping approach for turbulent partially premixed combustion. *Flow Turbul Combust* 2013;90(2):285–99.
- [34] Jangi M, Bai X-S. Multidimensional chemistry coordinate mapping approach for combustion modelling with finiterate chemistry. *Combust Theor Model* 2012;16:1109–32.
- [35] Jangi M, Altarawneh M, Glugogorski BZ. Large-eddy simulation of methanol pool fires using an accelerated stochastic fields method. *Combust Flame* 2016;173:89–98.
- [36] Pang KM, Jangi M, Bai X-S, Walther JH, Schramm J. Modelling of diesel spray flames under engine-like conditions using an accelerated Eulerian stochastic fields method. *Combust Flame* 2018;183:363–83.
- [37] Brookes S, Moss J. Predictions of soot and thermal radiation properties in confined turbulent jet diffusion flames. *Combust Flame* 1999;116:486–503.
- [38] Zhang M, Ong JC, Pang KM, Bai X-S, Walther JH. An investigation on early evolution of soot in n-dodecane spray combustion using large eddy simulation. *Fuel* 2021;293:120072.
- [39] Pope SB. Ten questions concerning the large-eddy simulation of turbulent flows. *New J Phys* 2004;6:1–24.
- [40] Pei Y, Hawkes ER, Kook S. A comprehensive study of effects of mixing and chemical kinetic models on predictions of n-heptane jet ignitions with the PDF method. *Flow Turbul Combust* 2013;91(2):249–80.
- [41] Pickett LM, Manin J, Genzale CL, Siebers DL, Musculus MPB, Idicheria C. Relationship between diesel fuel spray vapor penetration/dispersion and local fuel mixture fraction. *SAE Trans* 2011. 01-0686.
- [42] Payri R, Viera JP, Gopalakrishnan V, Szymkowitz PG. The effect of nozzle geometry over internal flow and spray formation for three different fuels. *Fuel* 2016;183:20–33.
- [43] Pei Y, Som S, Pomraning E, Senecal PK, Skeen SA, Manin J, Pickett LM. Large eddy simulation of a reacting spray flame with multiple realizations under compression ignition engine conditions. *Combust Flame* 2015;162:4442–55.
- [44] Pang KM, Poon HM, Ng HK, Gan S, Schramm J. Soot formation modeling of n-dodecane and diesel sprays under engine-like conditions. *SAE Trans* 2015.
- [45] Skeen SA, Manin J, Pickett LM, Cenker E, Bruneaux G, Kondo K, Aizawa T, Westlye F, Dalen K, Ivarsson A, et al. A progress review on soot experiments and modeling in the engine combustion network (ECN). *SAE Int J Engines* 2016;9(2):883–98.
- [46] Varna A, Wehrfritz A, Hawkes ER, Cleary MJ, Lucchini T, D'Errico G, Kook S, Chan QN. Using ducted fuel injection to attenuate or prevent soot formation in mixing-controlled combustion strategies for engine applications. *Proc Combust Inst* 2019;37:3263–70.
- [47] Fernandez SF, Paul C, Sircar A, Imren A, Haworth DC, Roy S, Modest MF. Soot and spectral radiation modeling for high-pressure turbulent spray flames. *Combust Flame* 2018;190:402–15.
- [48] Gehmlich R, Mueller C, Ruth D, Nilsen C, Skeen S, Manin J. Using ducted fuel injection to attenuate or prevent soot formation in mixing-controlled combustion strategies for engine applications. *Appl Energy* 2018;226:1169–86.
- [49] Pickett LM, Siebers DL. Soot in diesel fuel jets: effects of ambient temperature, ambient density, and injection pressure. *Combust Flame* 2004;138:114–35.
- [50] Glassman I. Soot formation in combustion processes. *Proc Combust Inst* 1989;22:295–311.
- [51] Nist. 2021, Available from: <https://www.nist.gov/>.
- [52] Beatrice C, Belardini P, Berteli C, Camerotti M, Cirillo N. Fuel jet models for multidimensional diesel combustion calculation: an update. *SAE Trans* 1995;194–204.
- [53] Omidvar A. Development and assessment of an improved droplet breakup model for numerical simulation of spray in a turbulent flow field. *Appl Therm Eng* 2019;156:432–43.